RSC Applied Interfaces

PAPER

View Article Online
View Journal | View Issue

Cite this: *RSC Appl. Interfaces*, 2025, **2**, 179

Oxalate-assisted Fe_2O_3 surface functionalization of nanosized $MgMn_2O_4$ and α-MnO_2 cathodes for rechargeable magnesium batteries†

Masanao Ishijima, *[a] Arisa Omata,[a] Kiyoshi Kanamura,[a] Toshihiko Mandai, [b] Xiatong Ye,[c] Tetsu Ichitsubo [c] and Koichi Kajihara *[a]

Received 15th August 2024,
Accepted 21st October 2024

DOI: 10.1039/d4lf00290c

rsc.li/RSCApplInter

Mn-based transition metal oxide nanoparticles are promising candidates as cathode active materials for rechargeable magnesium batteries, but their high catalytic activity for oxidative electrolyte decomposition and large surface area deteriorate their cycle performance. A recent study [Yagi *et al.*, *J. Mater. Chem. A*, 2021, **9**, 26401–26409] demonstrated that the catalytic activity was less prominent in Fe-based oxides than in other transition metal oxides, containing Mn. Fe-based oxides show low catalytic activity for oxidative electrolyte decomposition compared with Mn-based congeners. The strong capability of oxalate ions for bridging transition metal ions was utilised to form thin, uniform Fe_2O_3 layers on nanoparticles of $MgMn_2O_4$ and α-MnO_2. The resulting Fe_2O_3 layers effectively suppressed side reactions during insertion and extraction of the Mg^{2+} ions and improved the capacity retention and cycle performance.

Introduction

Rechargeable magnesium batteries (RMBs) have attracted increasing attention as advanced rechargeable batteries, because magnesium is an abundant element and magnesium metal anodes have high theoretical capacities (volumetric: 3833 mA h cm^{-3}, gravimetric: 2205 mA h g^{-1}). Promising cathode active materials for 3 V-class RMBs include hollandite-type α-MnO_2,[1–4] spinel-type MgM_2O_4 (M: transition metal),[5–7] and $ZnMnO_3$.[8–10] Electrolytes compatible with both magnesium metal anodes and transition metal oxide cathodes are presently limited to glyme-based electrolytes.[9] Despite the high catalytic activity of transition metal oxide cathodes containing Mn or Co, the oxidative decomposition of the glyme-based electrolytes on their surfaces during the extraction of Mg^{2+} ions is a crucial problem.[11,12] Such side reactions can be suppressed by passivating the surface active sites, where coating the surface of the cathode active materials with inert oxides (*e.g.*, V_2O_5 (ref. 13) or ZrO_2 (ref. 14)) or electroconductive polymers[15,16] has been reported to improve their electrochemical properties. On the other hand, recent studies have shown that oxidative electrolyte decomposition is less prominent on $MgFe_2O_4$ than on $MgMn_2O_4$ and $MgCo_2O_4$, indicating that the catalytic activity of Fe for oxidative electrolyte decomposition is lower than that of Mn and Co.[11] The partial substitution of Fe into Mn and Co sites (*e.g.*, $Mg(Co_{0.4}Fe_{0.6})O_4$ (ref. 12)) and coating of the surfaces of $MgMn_2O_4$ with Mg–Fe binary oxides[17] also improved the electrochemical properties.

The diffusion of divalent Mg^{2+} ions in the transition metal oxides is sluggish because of the strong electrostatic interactions between the Mg^{2+} ions and the oxide sublattice. To minimize the diffusion length of Mg^{2+} ions and facilitate their insertion and extraction, oxide-based RMB cathode materials with nanosized dimensions and large surface areas, such as 3D-open channel nanostructures (structured $MgMn_2O_4$ (ref. 18)) and ultrasmall (<2.5 nm) cubic $MgMn_2O_4$,[5] have been utilized. Surface functionalization *via* self-organization of reagents on the surface of transition metal oxides is an ideal way to form thin, uniform, and dense layers on transition metal oxides with large surface areas. As an example of such a self-organizing process, we developed the phenyl phosphonate surface functionalization of structured $MgMn_2O_4$ by utilizing the strong binding of the phenylphosphonate groups to the surface of transition metal oxides.[19]

Herein, we present another self-organizing process to form a thin Fe_2O_3 layer on nanosized transition metal oxide-based RMB cathode materials by employing oxalate ions, which are small polydentate ligands commonly used to form uniform

[a] *Department of Applied Chemistry for Environment, Graduate School of Urban Environmental Sciences, Tokyo Metropolitan University, Hachioji, Tokyo 192-0397, Japan. E-mail: ishijima@tmu.ac.jp, kkaji@tmu.ac.jp*
[b] *Research Center for Energy and Environmental Materials (GREEN), National Institute for Materials Science (NIMS), 1-1 Namiki, Tsukuba, Ibaraki 305-0044, Japan*
[c] *Institute for Materials Research, Tohoku University, Sendai 980-8577, Japan*

† Electronic supplementary information (ESI) available: Three electrode cell details, capacity retention and Coulombic efficiency of the cathode materials. See DOI: https://doi.org/10.1039/d4lf00290c

precipitates of multicomponent metal ions for the precursors of multicomponent ceramics.[20,21] The cathode active materials functionalized with oxalate ions were formed by treating in a solution of oxalate ions. They were converted to ones functionalized with Fe_2O_3 through treatment in a solution of iron(III) ions and subsequent heat treatment. The electrochemical properties of the resulting Fe_2O_3-functionalized cathode materials are presented.

Experimental

Synthesis of $MgMn_2O_4$

The structured $MgMn_2O_4$ powder was prepared by following a reported procedure.[18,19] Magnesium chloride hexahydrate ($MgCl_2{\cdot}6H_2O$, 6 mmol, Fujifilm Wako Pure Chemical), manganese chloride tetrahydrate ($MnCl_2{\cdot}4H_2O$, 12 mmol, Fujifilm Wako Pure Chemical), and citric acid (18 mmol, Fujifilm Wako Pure Chemical) were dissolved in 20 mL of ethanol, and propylene oxide (16 mL, Kanto Chemical) was added. The resulting metal–organic complex gel was maintained for 1 day at 25 °C, washed with ethanol and acetone to remove byproducts, and subjected to sequential solvent exchange with acetone for 1 day and cyclohexane 3 times in 3 days. The resulting wet gel was dried at 60 °C and heat treated at 350 °C for 5 h in a tube furnace in air.

Synthesis of α-MnO_2

The α-MnO_2 powder was prepared by following a reported procedure.[22–24] Manganese sulfate pentahydrate ($MnSO_4{\cdot}5H_2O$, 67 mmol, Fujifilm Wako Pure Chemical), ammonium sulfate ($(NH_4)_2SO_4$, 125 mmol, Fujifilm Wako Pure Chemical), and ammonium peroxydisulfate ($(NH_4)_2S_2O_8$, 67 mmol, Fujifilm Wako Pure Chemical) were dissolved in 100 mL of distilled water. The solution was then transferred to a Teflon-lined stainless-steel autoclave and heated at 140 °C for 12 h in an oven. The product was washed with an acetonitrile solution of nitronium tetrafluoroborate (NO_2BF_4, Fujifilm Wako Pure Chemical).

Fe_2O_3 functionalization

Ammonium oxalate monohydrate ($(NH_4)_2ox{\cdot}H_2O$, 0.25 mmol, Fujifilm Wako Pure Chemical) was dissolved in 3 g of distilled water. $MgMn_2O_4$ or α-MnO_2 (0.625 mmol) was added to the solution, and the suspension was stirred at room temperature for 3 h. The solid powder was separated by centrifugation, washed with water, and dried at 60 °C for 12 h. The dried solid powder was redispersed in a solution prepared by dissolving iron(III) nitrate nonahydrate ($Fe(NO_3)_3{\cdot}9H_2O$, Fujifilm Wako Pure Chemical) in 3 g of methanol (Fujifilm Wako Pure Chemical) at a molar ratio of $MgMn_2O_4$ or α-MnO_2 : $Fe(NO_3)_3$ = 1 : x, and the suspension was stirred at room temperature for 3 h. The solid powder was separated by centrifugation, washed with methanol, dried at 60 °C for 12 h, and heat treated at 350 °C for 5 h in a tube furnace in air.

Characterization

The resulting powder samples were evaluated by powder X-ray diffraction (XRD, SmartLab, Rigaku), Fourier-transform infrared (FT-IR) spectrometry (FT/IR-4600, JASCO) using an attenuated total reflection (ATR) unit with a diamond prism, scanning electron microscopy with energy-dispersive X-ray spectroscopy (SEM-EDS, PhenomPro, Thermo Fisher Scientific), and scanning transmission electron microscopy with EDS (STEM-EDS, JEM-ARM200F NEOARM, JEOL).

Electrochemical analysis

Dry composite cathodes were prepared by mixing the powder of pristine or Fe_2O_3-functionalized $MgMn_2O_4$ or α-MnO_2, acetylene black (AB, Denka; electrically conductive support), and poly(tetrafluoroethylene) (PTFE, Du Pont-Mitsui Fluorochemicals; binder) in a mass ratio of 60 : 30 : 10, and pressing ~2 mg of the composite with ~1.2 mg of cathode active material onto an Al mesh. Electrochemical measurements of the composite cathode were conducted in an Ar-filled glovebox with a three-electrode cell (Fig. S1†) using a Mg ribbon (99.9%, Yoneyama Yakuhin Kogyo) as the counter electrode, and a Ag wire immersed in a triglyme (G3, Kanto Chemical) solution of 0.01 mol dm^{-3} $AgNO_3$ (Kanto Chemical) and 0.1 mol dm^{-3} magnesium bis(trifluoromethanesulfonyl) amide ($Mg[TFSA]_2$, Kishida Chemical) as the reference electrode. The electrolytes used were 0.3 mol dm^{-3} [Mg(G4)] $[TFSA]_2$/$[C_3mPyr][TFSA]$,[25,26] prepared from tetraglyme (G4, Kishida Chemical), $Mg[TFSA]_2$, and 1-methyl-1-propylpyrrolidinium bis(trifluoromethanesulfonyl)amide ($[C_3mPyr][TFSA]$, Tokyo Chemical Industry), and 0.3 mol dm^{-3} G3 solution of magnesium tetrakis(hexafloroisopropyloxy)borate ($Mg[B(HFIP)_4]_2$).[27–29] Galvanostatic charge–discharge and galvanostatic intermittent titration technique (GITT) tests were carried out using electrochemical analyzers (HZ-Pro and HJ1020mSD8, Hokuto Denko) at 10 mA g^{-1} in the potential range from −1.6 to 0.9 V *vs.* Ag/Ag^+ (from 1.0 to 3.5 V *vs.* Mg/Mg^{2+}). The test was initiated from the discharge step, and the charge capacity was restricted to 180 mA h g^{-1} for $MgMn_2O_4$ and 200 mA h g^{-1} for α-MnO_2 (approximately two-thirds of the theoretical capacities of $MgMn_2O_4$ (270 mA h g^{-1})[5] and α-MnO_2 (308 mA h g^{-1})[30]). The rest period of the GITT measurements was 2 h.

Results and discussion

Structural characterization

Fig. 1 shows a schematic illustration of the Fe_2O_3 functionalization process. First, the surface of a cathode active material was modified with oxalate ions by suspending them in an aqueous ammonium oxalate solution. Fe^{3+} ions were anchored to the surfaces of the resulting samples by treatment with a methanol solution of iron(III) nitrate. Finally, oxalate ions and residual nitrate ions were

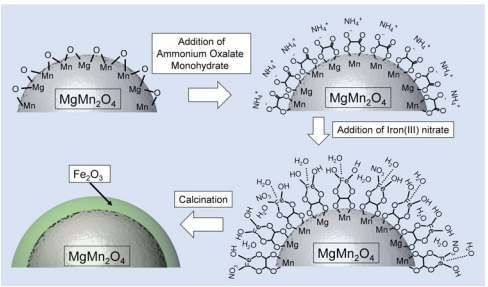

Fig. 1 Schematic illustration of the Fe_2O_3 functionalization process in the oxalate-assisted method.

decomposed by heat treatment to form thin uniform Fe_2O_3 layers on the structured $MgMn_2O_4$.

Fig. 2(a) shows the powder XRD patterns of the pristine and Fe_2O_3-functionalized $MgMn_2O_4$. The observed pattern of the pristine sample was essentially identical to those reported previously.[18,19,31,32] The similarity of the patterns before and after Fe_2O_3 functionalization indicated that the growth of $MgMn_2O_4$ crystallites and other crystalline phases during heat treatment was insignificant. Fig. 2(b) shows the ATR-FT-IR spectra of the $MgMn_2O_4$ powders during the course of Fe_2O_3 functionalization. The shoulder at ~650 cm^{-1} was attributed to the Mn–O stretching mode of the $MgMn_2O_4$.[33] After treatment with the ammonium oxalate solution (green line), absorption bands attributed to the oxalate ions were observed at ~1320, ~1375, and ~1650 cm^{-1},[34–36] and the ammonium ions were observed at ~1450 cm^{-1}.[37] After treatment with the iron(III) nitrate solution (blue line), absorption bands attributed to the nitrate ions appeared at ~1040 and ~1350 cm^{-1},[37] where the broad absorption band peaked at ~3300 cm^{-1}, originating from the O–H stretching mode of FeOH groups and adsorbed or coordinated water molecules, became prominent. In the spectrum of the Fe_2O_3-functionalized sample after heat treatment (red line), the absorption bands attributed to the oxalate, nitrate, and OH groups disappeared almost completely. Fig. 2(c) shows the SEM-EDS spectra of the pristine and Fe_2O_3-functionalized $MgMn_2O_4$. The Fe Kβ line was observed only in the spectrum of Fe_2O_3-functionalized $MgMn_2O_4$, and intensified with increasing x. Fig. 2(d) shows the STEM-EDS elemental mapping images of the Fe-functionalized $MgMn_2O_4$, verifying the uniform distribution of Fe on the particles.

To demonstrate the versatility of this method, Fe_2O_3 functionalization was applied to α-MnO_2. Fig. 3 shows the powder XRD patterns and SEM-EDS spectra of α-MnO_2 before and after Fe_2O_3 functionalization. Fe_2O_3 functionalization preserved the XRD patterns, whereas the Fe Kβ line appeared only in the spectrum of the Fe_2O_3-functionalized sample, similar to the structured $MgMn_2O_4$ shown in Fig. 2.

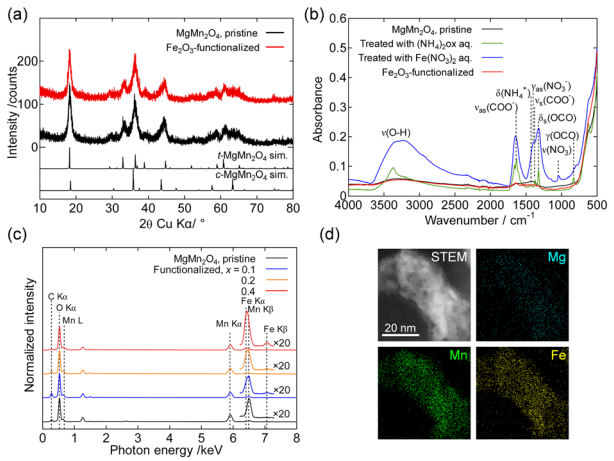

Fig. 2 (a) Powder XRD patterns of the pristine and Fe_2O_3-functionalized structured $MgMn_2O_4$ powders. Simulated patterns were calculated using RIETAN-FP[38] and the structure parameters of $MgMn_2O_4$ reported in ref. 31. (b) ATR-FT-IR spectra of the pristine structured $MgMn_2O_4$ powder after treatment with ammonium oxalate or iron(III) nitrate solution, and after heat treatment at 350 °C for 5 h in air (Fe_2O_3-functionalized sample). (c) SEM-EDS spectra of pristine and Fe_2O_3-functionalized structured $MgMn_2O_4$ powders. (d) STEM and EDS elemental mapping (Mg, Mn, and Fe) images of Fe_2O_3-functionalized structured $MgMn_2O_4$.

Electrochemical characterization

Fig. 4 shows the galvanostatic charge–discharge curves of the dry composite cathodes of the pristine and Fe_2O_3-functionalized $MgMn_2O_4$ powders. The current density was normalized to the mass of $MgMn_2O_4$ powder, including that of Fe_2O_3. For the pristine sample (Fig. 4(a)), the 1st charge cycle ended at ~2.9 V *vs.* Mg/Mg^{2+}, whereas the charge potential notably increased with cycle number. This potential increase was probably due to oxidative electrolyte decomposition and the simultaneous increase in the overpotential associated with the accumulation of decomposed products on the $MgMn_2O_4$ surface. Such an increase in the charge overvoltage with the number of cycles was significantly suppressed by surface functionalization with Fe_2O_3.

The initial discharge capacity was comparable for the pristine sample (~230 mA h g^{-1}) and those functionalized with Fe_2O_3 (~210, ~230, and ~240 mA h g^{-1} at x = 0.1, 0.2,

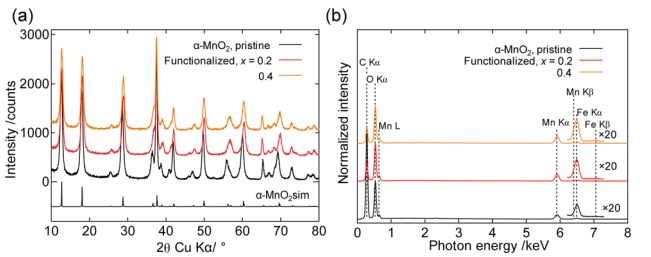

Fig. 3 (a) Powder XRD patterns of pristine and Fe_2O_3-functionalized α-MnO_2 powders. Simulated pattern was calculated using RIETAN-FP,[38] and the structure parameters of α-MnO_2 reported in ref. 39. (b) SEM-EDS spectra of pristine and Fe_2O_3-functionalized α-MnO_2 powders.

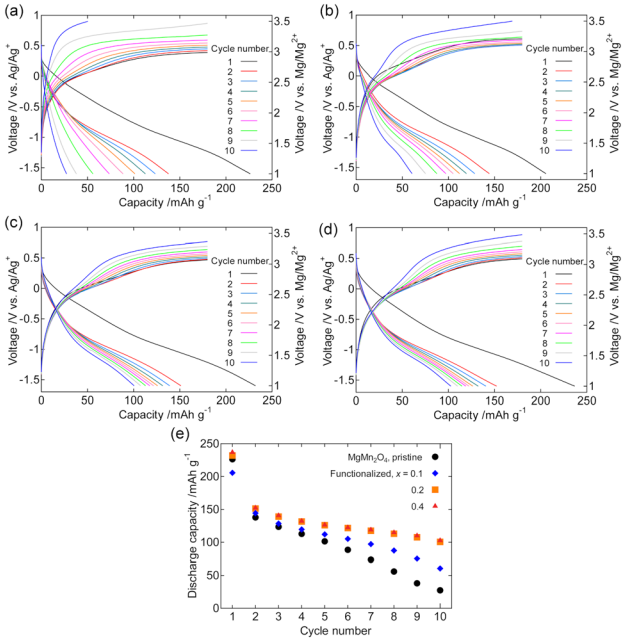

Fig. 4 Galvanostatic charge–discharge curves of dry composite cathodes of pristine $MgMn_2O_4$ (a) and those functionalized with Fe_2O_3 at x = 0.1 (b), 0.2 (c), and 0.4 (d) in 0.3 mol dm^{-3} [Mg(G4)][TFSA]$_2$/[C$_3$mPyr][TFSA] at 100 °C. (e) Discharge capacity retention of samples shown in panels (a)–(d).

and 0.4, respectively). The decay in the discharge capacity between the 1st and 2nd cycles was mainly due to the incomplete extraction of Mg^{2+} ions during the 1st charge cycle. In the pristine sample, the discharge capacity rapidly deteriorated with cycle number. This discharge capacity fading was also suppressed by the Fe_2O_3 functionalization. Fig. 4(e) and S2† show the discharge capacity retention and Coulombic efficiency. The discharge capacity after the 10th cycle was ~100 mA h g^{-1} for the samples with x = 0.2 and 0.4, and was notably higher than that of the pristine sample (~25 mA h g^{-1}). Coulombic efficiency derived as the ratio of the discharge capacity to the charge capacity of the previous cycle, was also improved and exhibited ~0.6 at the 10th cycle for samples with x = 0.2 and 0.4.

Fig. 5 and S3† show the galvanostatic charge–discharge curves, discharge capacity retention, and Coulombic efficiency of the composite cathodes of pristine and Fe_2O_3-functionalized α-MnO_2 (x = 0.2, and 0.4) in [Mg(G4)][TFSA]$_2$/[C$_3$mPyr][TFSA] at 100 °C. Similar to structured $MgMn_2O_4$, Fe_2O_3 functionalization suppressed the increase in the charge potential with cycle number, and improved discharge capacity retention. The GITT profiles of the same composite cathodes are shown in Fig. 6. The amplitude of transient potential change was comparable in the 1st cycle, whereas smaller in the Fe_2O_3-functionalized sample in the 5th cycle. This observation indicates the reduction of overpotentials during charging and discharging by the Fe_2O_3 functionalization. Fig. 7 and S4† show the galvanostatic charge–discharge curves, discharge capacity retention, and Coulombic efficiency of the composite cathodes of pristine and Fe_2O_3-functionalized α-MnO_2 in Mg[B(HFIP)$_4$]$_2$/G3 at 30 °C. In the pristine sample, the potential reached to the upper bound (3.5 V *vs.* Mg/Mg^{2+}) during charging, indicating a large overpotential. In the Fe_2O_3-functionalized samples, the overpotential during charging was suppressed, and discharge capacity for up to the 5–6 cycles was significantly improved. The rapid fading of the discharge capacity thereafter in the Fe_2O_3-functionalized samples may be due to the reduced mobility of Mg^{2+} ions at 30 °C and the vulnerability of transition metal oxides to reduction in solvent (glyme)-rich electrolytes, both of which favour the destruction of α-MnO_2 crystallites rather than the reversible insertion and extraction of Mg^{2+} ions. Coulombic efficiency at the 10th cycle of the Fe_2O_3-functionalized samples with x = 0.4 was ~0.8 both in [Mg(G4)][TFSA]$_2$/[C$_3$mPyr][TFSA] and Mg[B(HFIP)$_4$]$_2$/G3, and better than other two samples.

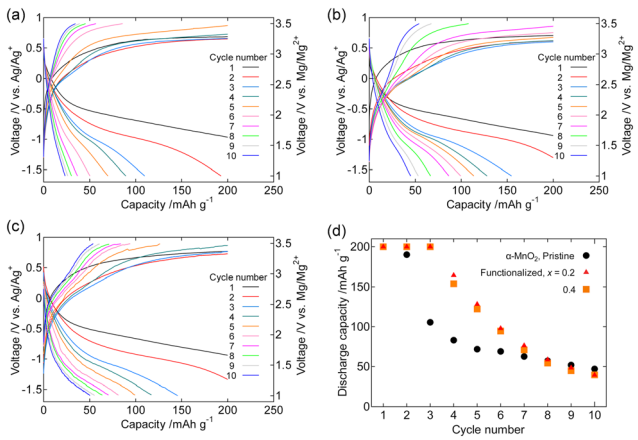

Fig. 5 Galvanostatic charge–discharge curves of dry composite cathodes of the pristine α-MnO_2 (a), and those functionalized with Fe_2O_3 at x = 0.2 (b) and 0.4 (c) in 0.3 mol dm^{-3} [Mg(G4)][TFSA]$_2$/[C$_3$mPyr][TFSA] at 100 °C. (d) Discharge capacity retention of samples shown in panels (a)–(c).

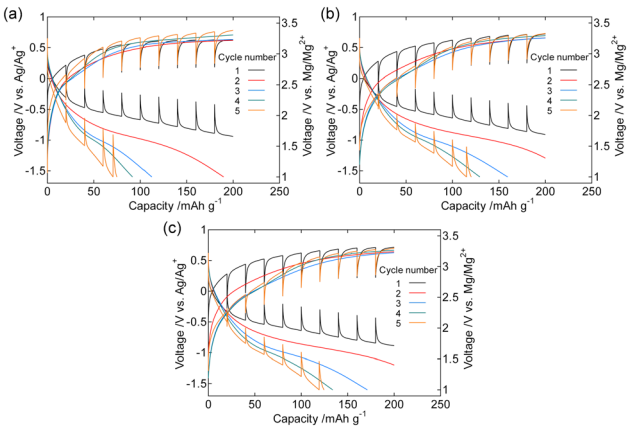

Fig. 6 GITT profiles of the pristine α-MnO_2 (a), and those functionalized with Fe_2O_3 at x = 0.2 (b) and 0.4 (c) in 0.3 mol dm^{-3} [Mg(G4)][TFSA]$_2$/[C$_3$mPyr][TFSA] at 100 °C.

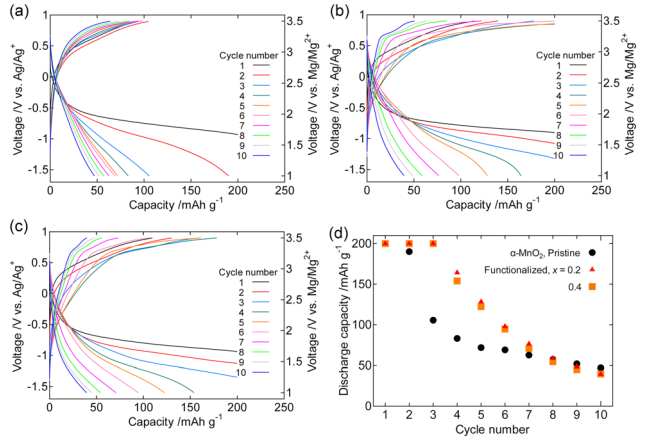

Fig. 7 Galvanostatic charge–discharge curves of dry composite cathodes of the pristine α-MnO_2 (a), and those functionalized with Fe_2O_3 at x = 0.2 (b) and 0.4 (c) in 0.3 mol dm^{-3} $Mg[B(HFIP)_4]_2$/G3 at 30 °C. (d) Discharge capacity retention of samples shown in panels (a)–(c).

Conclusions

An oxalate-assisted Fe_2O_3 functionalization technique was developed for the surface modification of nanosized transition metal oxides ($MgMn_2O_4$ and α-MnO_2) with large surface areas as cathode active materials for RMBs. Oxalate ions worked as efficient bridging agents between iron(III) ions and the surface of transition metal oxides. Fe_2O_3 functionalization suppressed side reactions including oxidative electrolyte decomposition, decreased overpotentials during charging and discharging, and improved discharge capacity retention. These observations demonstrate that the oxalate-assisted Fe_2O_3 functionalization is one of the powerful self-organizing surface functionalization techniques for the improvement of the electrochemical properties of cathode active materials for RMBs.

Data availability

The data of this study are available from the corresponding authors upon reasonable request.

Conflicts of interest

There are no conflicts to declare.

Acknowledgements

This work was supported by GteX Program Japan Grant Number JPMJGX23S1. The authors thank Dr. Yuma Shimbori for assistance with electrochemical measurements, and Mr. Yuki Ono of Tokyo Metropolitan University for providing valuable technical support during the STEM-EDS observations.

References

1 X. Guo, S. Yang, D. Wang, A. Chen, Y. Wang, P. Li, G. Liang and C. Zhi, *Curr. Opin. Electrochem.*, 2021, **30**, 100769.
2 J. Shin, J. K. Seo, R. Yaylian, A. Huang and Y. S. Meng, *Int. Mater. Rev.*, 2020, **65**, 356–387.
3 C. Yuan, Y. Zhang, Y. Pan, X. Liu, G. Wang and D. Cao, *Electrochim. Acta*, 2014, **116**, 404–412.
4 X. Ye, H. Li, T. Hatakeyama, H. Kobayashi, T. Mandai, N. L. Okamoto and T. Ichitsubo, *ACS Appl. Mater. Interfaces*, 2022, **14**, 56685–56696.
5 H. Kobayashi, Y. Fukumi, H. Watanabe, R. Iimura, N. Nishimura, T. Mandai, Y. Tominaga, M. Nakayama, T. Ichitsubo, I. Honma and H. Imai, *ACS Nano*, 2023, **17**, 3135–3142.
6 J. Yin, A. B. Brady, E. S. Takeuchi, A. C. Marschilok and K. J. Takeuchi, *Chem. Commun.*, 2017, **53**, 3665–3668.
7 G. Liu, Q. Chi, Y. Zhang, Q. Chen, C. Zhang, K. Zhu and D. Cao, *Chem. Commun.*, 2018, **54**, 9474–9477.
8 T. Mandai, A. Kutsuma, M. Konya, Y. Nakabayashi and K. Kanamura, *Electrochemistry*, 2022, **90**, 027005.
9 S. Okamoto, T. Ichitsubo, T. Kawaguchi, Y. Kumagai, F. Oba, S. Yagi, K. Shimokawa, N. Goto, T. Doi and E. Matsubara, *Adv. Sci.*, 2015, **2**, 1500072.
10 K. Shimokawa, T. Atsumi, M. Harada, R. E. Ward, M. Nakayama, Y. Kumagai, F. Oba, N. L. Okamoto, K. Kanamura and T. Ichitsubo, *J. Mater. Chem. A*, 2019, **7**, 12225–12235.
11 J. Han, S. Yagi, H. Takeuchi, M. Nakayama and T. Ichitsubo, *J. Mater. Chem. A*, 2021, **9**, 26401–26409.
12 J. Han, S. Yagi, H. Takeuchi, M. Nakayama and T. Ichitsubo, *J. Phys. Chem. C*, 2022, **126**, 19074–19083.
13 S. Doi, R. Ise, T. Mandai, Y. Oaki, S. Yagi and H. Imai, *Langmuir*, 2020, **36**, 8537–8542.
14 N. Kitamura, T. Imura, N. Ishida, C. Ishibashi and Y. Idemoto, *ACS Omega*, 2022, **7**, 46915–46921.
15 N. Nishimura, K. Masaki, W. Tan, R. Iimura, H. Kobayashi, K. Nishikawa, T. Mandai, H. Somekawa and Y. Tominaga, *J. Phys. Chem. C*, 2023, **127**, 11829–11835.
16 N. Nishimura, K. Masaki, K. Nishikawa, Y. Idemoto and Y. Tominaga, *Chem. Lett.*, 2023, **52**, 89–92.
17 R. Iimura, H. Kobayashi and I. Honma, *Electrochemistry*, 2022, **90**, 067002.
18 K. Sone, Y. Hayashi, T. Mandai, S. Yagi, Y. Oaki and H. Imai, *J. Mater. Chem. A*, 2021, **9**, 6851–6860.
19 K. Kajihara, D. Takahashi, H. Kobayashi, T. Mandai, H. Imai and K. Kanamura, *RSC Adv.*, 2021, **11**, 19076–19082.
20 D.-Q. Zhang, Z.-C. Qin, X.-Y. Yang, H.-B. Zhu and M.-S. Cao, *J. Sol-Gel Sci. Technol.*, 2011, **57**, 31–35.
21 Y.-J. Hao, Q.-Y. Lai, J.-Z. Lu, H.-L. Wang, Y.-D. Chen and X.-Y. Ji, *J. Power Sources*, 2006, **158**, 1358–1364.
22 X. Wang and Y. Li, *J. Am. Chem. Soc.*, 2002, **124**, 2880–2881.
23 T. Hatakeyama, N. L. Okamoto and T. Ichitsubo, *J. Solid State Chem.*, 2022, **305**, 122683.

24 T. Hatakeyama, H. Li, N. L. Okamoto, K. Shimokawa, T. Kawaguchi, H. Tanimura, S. Imashuku, M. Fichtner and T. Ichitsubo, *Chem. Mater.*, 2021, **33**, 6983–6996.
25 S. Terada, T. Mandai, S. Suzuki, S. Tsuzuki, K. Watanabe, Y. Kamei, K. Ueno, K. Dokko and M. Watanabe, *J. Phys. Chem. C*, 2016, **120**, 1353–1365.
26 T. Mandai, K. Tatesaka, K. Soh, H. Masu, A. Choudhary, Y. Tateyama, R. Ise, H. Imai, T. Takeguchi and K. Kanamura, *Phys. Chem. Chem. Phys.*, 2019, **21**, 12100–12111.
27 T. Mandai, *ACS Appl. Mater. Interfaces*, 2020, **12**, 39135–39144.
28 Z. Zhang, Z. Cui, L. Qiao, J. Guan, H. Xu, X. Wang, P. Hu, H. Du, S. Li, X. Zhou, S. Dong, Z. Liu, G. Cui and L. Chen, *Adv. Energy Mater.*, 2017, **7**, 1602055.
29 Z. Zhao-Karger, M. E. Gil Bardaji, O. Fuhr and M. Fichtner, *J. Mater. Chem. A*, 2017, **5**, 10815–10820.
30 C. Ling, R. Zhang, T. S. Arthur and F. Mizuno, *Chem. Mater.*, 2015, **27**, 5799–5807.
31 S. Yagi, Y. Ichikawa, I. Yamada, T. Doi, T. Ichitsubo and E. Matsubara, *Jpn. J. Appl. Phys.*, 2013, **52**, 025501.
32 K. Ishii, S. Doi, R. Ise, T. Mandai, Y. Oaki, S. Yagi and H. Imai, *J. Alloys Compd.*, 2020, **816**, 152556.
33 L. Malavasi, P. Galinetto, M. C. Mozzati, C. B. Azzoni and G. Flor, *Phys. Chem. Chem. Phys.*, 2002, **4**, 3876–3880.
34 K. Sarmah and S. Pratihar, *ACS Sustainable Chem. Eng.*, 2017, **5**, 310–324.
35 M. A. Gabal, *J. Mater. Res. Technol.*, 2021, **15**, 5841–5848.
36 M. A. Gabal, A. A. El-Bellihi and S. S. Ata-Allah, *Mater. Chem. Phys.*, 2003, **81**, 84–92.
37 H. B. Wu, M. N. Chan and C. K. Chan, *Aerosol Sci. Technol.*, 2007, **41**, 581–588.
38 F. Izumi and K. Momma, *Solid State Phenom.*, 2007, **130**, 15–20.
39 Y. D. Kondrashev and A. I. Zaslavskii, *Izv. Akad. Nauk SSSR, Ser. Fiz.*, 1951, **15**, 179–186.